Nanoscale
Advances

ROYAL SOCIETY
OF CHEMISTRY

PAPER

View Article Online
View Journal | View Issue

Check for updates

Cite this: *Nanoscale Adv.*, 2023, **5**, 711

A mucus-inspired solvent-free carbon dot-based nanofluid triggers significant tribological synergy for sulfonated h-BN reinforced epoxy composites†

Chengcheng Jiao,[ab] Tao Cai, *[b] Huanyi Chen,[b] Xinxin Ruan,[b] Yandong Wang,[b] Ping Gong,[b] Hua Li,[c] Rob Atkin, [c] Feng Yang,*[a] Haichao Zhao, [b] Kazuhito Nishimura,[d] Nan Jiang[b] and Jinhong Yu *[b]

Received 7th October 2022
Accepted 8th December 2022

DOI: 10.1039/d2na00689h

rsc.li/nanoscale-advances

Nano-filler reinforced polymer-based composites have attracted extensive attention in tribology; however, to date, it is still challenging to construct a favorable lubricating system with excellent compatibility, lubricity and durability using nano-filler reinforced polymer-based composites. Herein, sulfonated boron nitride nano-sheets (h-BN@PSDA) are prepared and used as nano-fillers for epoxy resins (EPs), to improve friction and wear along with thermal conductivity. Furthermore, inspired by the lubricating principle and structure of snail mucus, a solvent-free carbon dot-based nanofluid (F-CDs) is fabricated and used for the first time as the lubricant for h-BN@PSDA/EPs. Both poly (4-styrene sulfonate) and polyether amine grafted on the surface of F-CDs contribute to branched structures and multiple interfacial absorption effects. Extraordinarily low friction and wear are detected after long-term sliding. The average coefficient of friction and wear rate of h-BN@PSDA/EPs composites are reduced by 95.25% and 99.42% respectively, in the presence of the F-CD nanofluid, compared to that of EPs. Besides, the added h-BN nano-sheets increase the thermal conductivity (TC) of EPs from 0.178 to 0.194 W (m^{-1} K^{-1}). The distinguished lubrication performances are likely due to the formation of a hybrid nanostructure of 0D F-CDs and 2D h-BN@PSDA together with the "rolling–sliding" and "self-mending" effects of added F-CDs.

Introduction

Polymer-based composites have a wide range of applications in vehicles, aerospace engineering, packaging, and marine equipment.[1–6] Recently, to increase the energy efficiency and reduce emission, polymer-based composites with long-term durability against friction and wear are urgently needed.[7–9] These required performances can be improved by mixing polymer-based composites with two-dimensional (2D) nanomaterials which have low inter-layer shear strength, excellent lubricity and high thermal conductivity.[10,11] As commonly used 2D materials, hexagonal boron nitride (h-BN) nano-sheets are composed of 2D layers of alternating boron and nitrogen atoms. They are analogues of graphene and exhibit ultra-high thermal conductivity and excellent tribological properties along with great mechanical strength.[12,13] However, compared to other typical 2D materials, h-BN nano-sheets are chemically inert, thereby interacting poorly with polymer matrixes. They are prone to agglomerate and stack with each other due to large specific surface areas and strong van der Waals interactions between layers, which lead to degraded performances and limited applications.[14,15] Previous studies have shown that the compatibility between nano-fillers and resin matrix and the tribological performances of the obtained composites can be improved by surface functionalization.[16–18] For example, hydroxylated h-BN has been found to disperse evenly in the resin matrix and improve the mechanical and tribological properties.[19] Organic coated h-BN and cubic-BN nano-fillers have shown improved dispersion in EPs, leading to enhanced tribological properties.[20] The use of hydrophobic SiC coated h-BN as nanofillers has improved both the friction and corrosion properties of EPs.[21,22] However, to date, the compatibility between h-BN nano-sheets and resin matrixes is still awaiting improvement owing to the extremely inert surface properties of h-BN nano-sheets, leading to complicated chemical modifications.

In addition to nano-fillers, the lubricating fluid also enhances the tribological performance and extends the lifetime

---

[a] School of Materials Science and Engineering, Shenyang University of Chemical Technology, Shenyang 110142, China. E-mail: yf18231@163.com

[b] Key Laboratory of Marine Materials and Related Technologies, Zhejiang Key Laboratory of Marine Materials and Protective Technologies, Ningbo Institute of Materials Technology and Engineering, Chinese Academy of Sciences, Ningbo 315201, China. E-mail: caitao@nimte.ac.cn; yujinhong@nimte.ac.cn

[c] School of Molecular Sciences, University of Western Australia, Perth, Western Australia, Australia

[d] Advanced Nano-Processing Engineering Lab, Mechanical Engineering, Kogakuin University, Tokyo, 192-0015, Japan

† Electronic supplementary information (ESI) available. See DOI: https://doi.org/10.1039/d2na00689h

of resin matrixes.[23,24] Ionic liquids (ILs) are salts with melting temperatures below 100 °C.[25–27] A well-adsorbed IL boundary lubrication film is formed at the sliding surface due to strong electrostatic, van der Waals, and H-bonding interactions to resist the contact between counter bodies and reduce friction and wear.[23,28] Furthermore, ILs have been combined with 2D nanomaterials to improve boundary layer adhesion and lubricity. Low friction and wear have been detected for PAO lubricants consisting of a phosphonium IL and graphene nanosheets/hexagonal boron nitride nanoparticles as lubricant additives due to the formation of the adsorbed IL film and the repairing effect of nano-sheets, which avoids direct contact at the interface.[29] For polymer-based composites containing IL functionalized graphene oxide, anions of ILs bonded with GO nano-sheets are released from the resin matrix and adsorbed firmly to the positively electrified parts of the steel surface, leading to the great increase of the interface adsorption abilities of IL functionalized graphene oxide and enhanced durability of the adsorption film against friction and wear.[30] Currently, traditional nanofluids containing IL hybrid nanomaterials are mainly explored as lubricant additives for hard counter bodies, such as metal/ceramic tribo-pairs. Polymer-based composites are relatively soft and brittle, thus are not feasible to be lubricated by liquids containing conventional nanomaterials, since abrasive wear may lead to increased wear.

In nature, the mucus secreted by the snail's body provides excellent lubricating properties to protect its body tissues from damage when wriggling and crawling on a variety of rough and sharp surfaces. The lubricating mechanism is that the mucus flows freely like liquids after absorption of sufficient water, and the glycoprotein and amino acids contained in the snail mucus form multiple adsorption networks on the surface, thus creating a stable and continuous lubricating film on the crawling surface. Carbon dots (CDs) are a new type of carbon-based nanomaterials with uniform sizes at the nanoscale (<10 nm). They have many advantages, such as good biocompatibility, photostability, low toxicity, high specific surface area, as well as easy preparation and functionalization, and thus attract increasing research interests.[31–35] Carbon dots are promising lubricant additives due to their extremely small dimensions, well-defined spherical structure and soft feature, which perform the "ball effect" and "self-healing" between counter bodies at the nanoscale, thereby reducing friction and wear up to high load.[36–38]

Here, bio-inspired by the snail mucus, for the first time we design an advanced lubricating system that combines the advantages of 2D materials, *cf.* h-BN, and a 0D carbon dot-based nanofluid to form a stable, homogeneous and continuous boundary film to effectively reduce friction and wear at polymer composite surfaces. Firstly, to increase the compatibility of h-BN nanosheets with the resin matrix, the originally chemically inserted h-BN nanosheets are pre-functionalized by a synthetic catecholic compound, sulfonated dopamine, to increase the electronegativity and hydrophilicity, and thus improve dispersion stability and compatibility with the resin matrix. Then a solvent-free carbon-dot based nanofluid with a 3D polyelectrolyte structure and multiple adsorption networks is fabricated and applied as the lubricant to boost the lubricity and durability of the boundary film. The potential lubrication mechanism is systematically studied by characterizing the friction pairs along with wear debris using surface analysis techniques.

Experimental

Materials

Hexagonal boron nitride (h-BN), citric acid monohydrate, ammonia solution, polyethylene glycol (PEG, M_w = 400 g mol^{-1}), and 1,3-propanesulfonate (1,3-PS) were acquired from Aladdin Reagent Co., Ltd (Shanghai, China). Dopamine hydrochloride (DA), epoxy resin (E51), tris-(hydroxymethyl)aminomethane (Tris) and the curing agent (D-230) were ordered from Macklin Biochemical Co., Ltd. Acetone, poly(4-styrene sulfonate), anhydrous ethanol, and concentrated hydrochloric acid were provided by Sinopharm Chemical Reagent Co., Ltd. Polyether amine (M_w = 2000 g mol^{-1}) was provided by Huntsman Co., Ltd (USA).

Preparation of sulfonated dopamine (SDA)

1.5 g dopamine hydrochloride was dispersed into 180 ml anhydrous ethanol, then 1.06 g 1.3-PS and 0.555 ml ammonia solution were slowly dripped in the dopamine hydrochloride dispersion. The reaction solution was reacted at 40–50 °C for 15 to 20 hours and then filtered. The solid phase was rinsed with anhydrous ethanol, followed by drying at 40 °C to obtain the dopamine sulfonate. The scheme of the chemical reaction process for synthesizing SDA is shown in Scheme 1.

Preparation of polysulfonated dopamine functionalized boron nitride (h-BN@PSDA)

0.1 g of h-BN nanosheets was weighed and dispersed in Tris–HCl solution. 0.1 g of SDA was then mixed with the h-BN dispersion followed by stirring for 10 h to obtain a homogeneous dispersion. Sulfonated dopamine could form a polysulfated dopamine (PSDA) layer that can attach to the surface of various substrates under oxygenated and alkaline conditions. The obtained solution was filtered to completely remove the residual SDA and PSDA. The filtered product was washed three times with ethanol and DI water and dried to obtain the h-BN@PSDA powders (Fig. 1) with a light grey color.

Fabrication of h-BN@PSDA/EP composites

Three sets of samples were prepared for comparison experiments (EPs, h-BN/EPs, h-BN@PSDA/EPs) with 0.6 wt% of h-BN in the composites (the fabricating processes of EP and h-BN/EPs are shown in the ESI†). The preparation process for h-BN@PSDA/EPs was as follows: h-BN@PSDA with a weight of

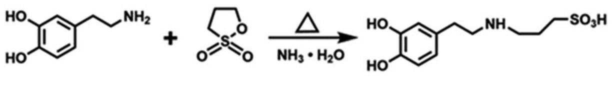

Scheme 1 Synthesis of sulfated dopamine.

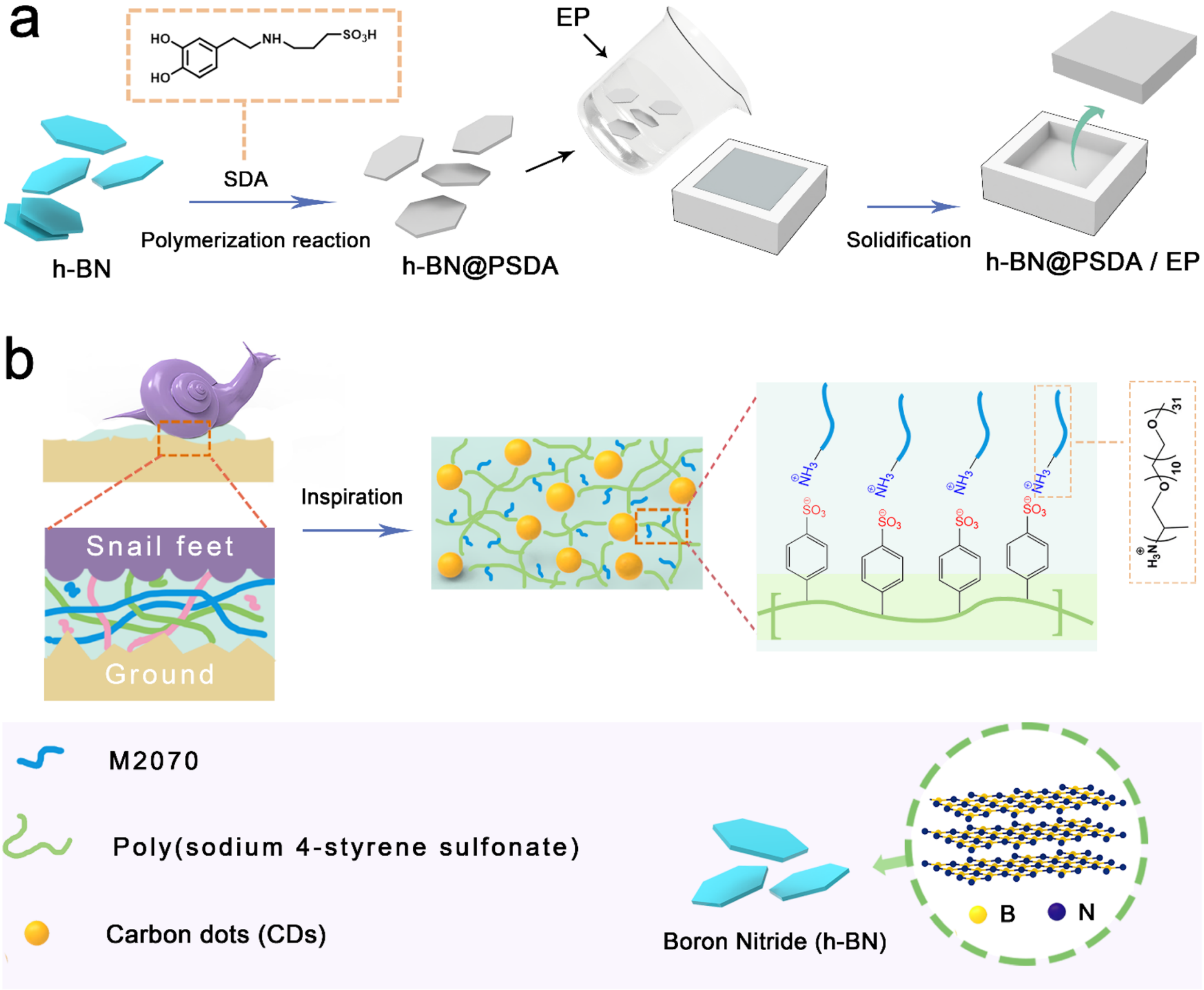

Fig. 1 (a) Synthesis process of h-BN@PSDA and h-BN@PSDA/EPs; (b) schematic diagram of a 3D polymer network on the surface of a solvent-free carbon dot nanofluid prepared inspired by the mucus lubrication system of a snail.

0.03 g was dispersed in acetone under sonication, subsequently by adding 5 g of EPs. The mixture was firstly mixed well with a blender. The major part of the solvent (acetone) was removed *via* evaporation in air under magnetic stirring, and the residue was removed in a vacuum oven. After solvent removal, 1.5 g of the curing agent was blended to the mixture using a Speedmixer (DAC150.1 FVZ-K, Germany). Finally, the resulting mixture was molded in a Teflon model after removing all the bubbles in a vacuum oven at ambient temperature. The h-BN@PSDA/EP composites were cured at 60 °C for 3 h, then at 80 °C for 12 h, and finally at 120 °C for another 2 h in an atmospheric pressure oven (Fig. 1).

Synthesis of solvent-free carbon dot-based ionic fluid

A two-step strategy was used to prepare the mucus-inspired carbon dot-based ionic liquid without any solvent. In the first step, we used the one-pot method to prepare the solid polyelectrolyte grafted carbon dots. The details can be seen below: a transparent solution was obtained through mixing the citric acid and poly (4-styrene sulfonate) with DI water, followed by removing the solvent *via* rotary evaporation. Then the target product can be obtained after pyrolysis at 200 °C for 2 hours. Secondly, we separated the residue after dissolving the prepared target product through filtration. The filtrate was dialyzed in a mixture of DI water and ethanol for 48 h to purify the as-prepared grafted carbon dots. The Na^+ is removed from the dialyzed solution using ion exchange resin until the pH of the solution is stable. Polyether amine is dissolved in deionized water, and then dropwise added for 60 minutes to the above aqueous solution containing carbon dots and the reaction mixture is stirred for 40 h after the dropwise addition is completed. Finally, dark red-brown viscous fluid carbon dots are obtained after removing the solvent by the rotary evaporation process.

Characterization

The molecular structures of SDA and DA were determined by nuclear magnetic resonance hydrogen spectroscopy (^1H NMR; AVANCE NEO, Germany). The morphology size of h-BN was characterized by atomic force microscopy using tapping mode with a silicon cantilever (AFM, Bruker Dimension ICON, USA). Contact angle tests of h-BN@PSDA and h-BN dispersions were performed on a CA contact angle tester (CA, DCAT21, China). Zeta potentials of h-BN and h-BN@PSDA nano-sheets were measured using a Zeta-sizer (Zeta; ZS ultra, Malvern Panalytical). Raman spectra of h-BN before and after functionalization were obtained using a Raman spectrometer (LabRAM Odysseyy, HORIBA FRANCE SAS). Ultraviolet-visible (UV-vis) spectra were obtained using a UV/VIS/NIR spectrophotometer (UV/VIS/NIR; Lambda 1050+, USA). X-ray diffraction was studied with an X-ray powder diffractometer (XRD; D8 ADVANCE, Germany). Thermogravimetric analysis (TGA; STA449 F3, Germany) was used to analyze the decomposition process of h-BN@PSDA. The elemental compositions of h-BN nano-sheets before and after chemical functionalization and the steel substrate after tribological tests were characterized by X-ray photoelectron spectroscopy (XPS; Axis Ultra DLD, UK). The morphologies of h-BN before and after functionalization were recorded using a scanning electron microscope at 10 kV (SEM; Regulus8230, Japan). The surface elemental analysis of h-BN@PSDA as well as the characterization of the morphology of CDs was performed with transmission electron microscopy (HR-TEM; Talos F200X, USA). The elemental composition of the cross-section of the lubricating film in the wear track was analyzed by focused ion beam scanning electron microscopy (FIB; Auriga, Germany) and TEM.

The tribological properties of the epoxy composite material were measured by means of reciprocating ball plane friction tests using a multi-functional high temperature tribometer (UMT-3, USA). GCr15 steel balls with a diameter of 6 mm were used as the upper friction substrate. The substrate for the bottom friction was an epoxy resin composite plate of 5 mm thickness, 3 mm length and 3 mm width. The specific friction test conditions included: load 5 N; frequency 5 Hz; amplitude 5.5 mm; duration 15–120 min. The friction coefficient curves were automatically monitored and recorded using a highly sensitive sensor connected to the UMT friction tester. The coefficient of friction was calculated as the average of all data points on the friction coefficient curve. The oil stains on the GCr15 balls were ultrasonically cleaned with anhydrous ethanol before testing. Wear rates (W_r) and wear areas were measured using a non-contact optical profilometer (Rtec Universal Profilometer; Rtec Up-Lambda, USA). The specific wear rate can be calculated using the following equation:

$$W_r = AL/F_nS \tag{1}$$

where A, L and S refer to the area of the depth profile, the length of wear tracks, and the sliding distance, respectively. A laser confocal microscope (VK-X1000, KEYENCE, Japan) was used to optically observe the morphology of the wear marks.

We used a laser flash apparatus (LFA; NETZSCH LFA 467, Germany) to test the thermal diffusivity of the epoxy composite. The specific heat capacity of all the samples was obtained by recording the differential scanning calorimeter (DSC; NETZSCH DSC 214, Germany) curve in a nitrogen atmosphere, and the density was obtained using an electron density balance. Thermal conductivity, K, was calculated from:

$$K = \alpha \times C_p \times \rho \tag{2}$$

where α, C_p, and ρ refer to thermal diffusivity ($mm^2\ s^{-1}$), specific heat ($J\ g^{-1}\ K^{-1}$), and density ($g\ cm^{-3}$), respectively.

Results and discussion

In Fig. 2a, the TEM image reveals that the fluid-like carbon dot-based ionic fluid has been successfully synthesized with an average particle diameter of 5.66 nm. The lattice spacing of 0.23 nm corresponding to the (100) facet of graphite is observed in the HR-TEM image (Fig. 2b inset). Fig. 2c demonstrates the excellent fluidity of the solvent-free carbon dot nanofluid. The ^{1}H NMR spectrum of the synthesized SDA is presented in Fig. 3a. Compared to raw DA, SDA shows new proton peaks at 2.01 (g), 2.89 (f) and 3.19 (h) ppm, respectively, which are attributed to the hydrogen atoms of the carbon chain (–CH_2–CH_2–CH_2–SO_3H) from the ring-opening reaction of 1,3-propanesulfonate and grafting reaction into the primary amine groups of DA.[39] AFM measurements show that h-BN nanosheets are circular thin sheets with a size of less than 150 nm and a thickness of about 8 nm (Fig. 3b and c). Mussel-inspired sulfonated dopamine (SDA) with abundant hydrophilic groups, which shows a universal adhesive ability to adhere to almost all organic and inorganic substrates, was applied to modify h-BN to improve its compatibility with resin substrates. Fig. 3d shows the Raman spectra of h-BN and h-BN@PSDA. The original h-BN shows a single and acute characteristic peak at 1364 cm^{-1}, resulting from the E_{2g} phonon pattern of h-BN. In contrast, h-BN@PSDA displays a much weaker peak at 1364 cm^{-1} and a new characteristic peak at 1597 cm^{-1}, attributed to the stretching vibration and deformation of catechol in the PSDA structure.[40] The zeta potential of h-BN is approximately

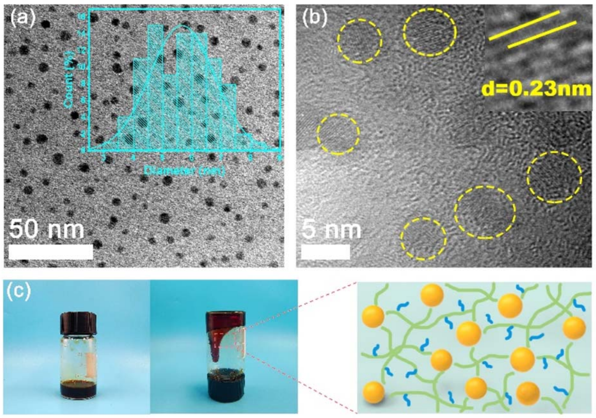

Fig. 2 (a) TEM with low resolution and (b) HR-TEM images of fluid-like carbon dots. The inset in (a) shows the particle size distribution of the solvent-free carbon dot nanofluid identified in yellow. (c) Flow schematic of the solvent-free carbon dot nanofluid and the mechanism of the polymeric three-dimensional network structure.

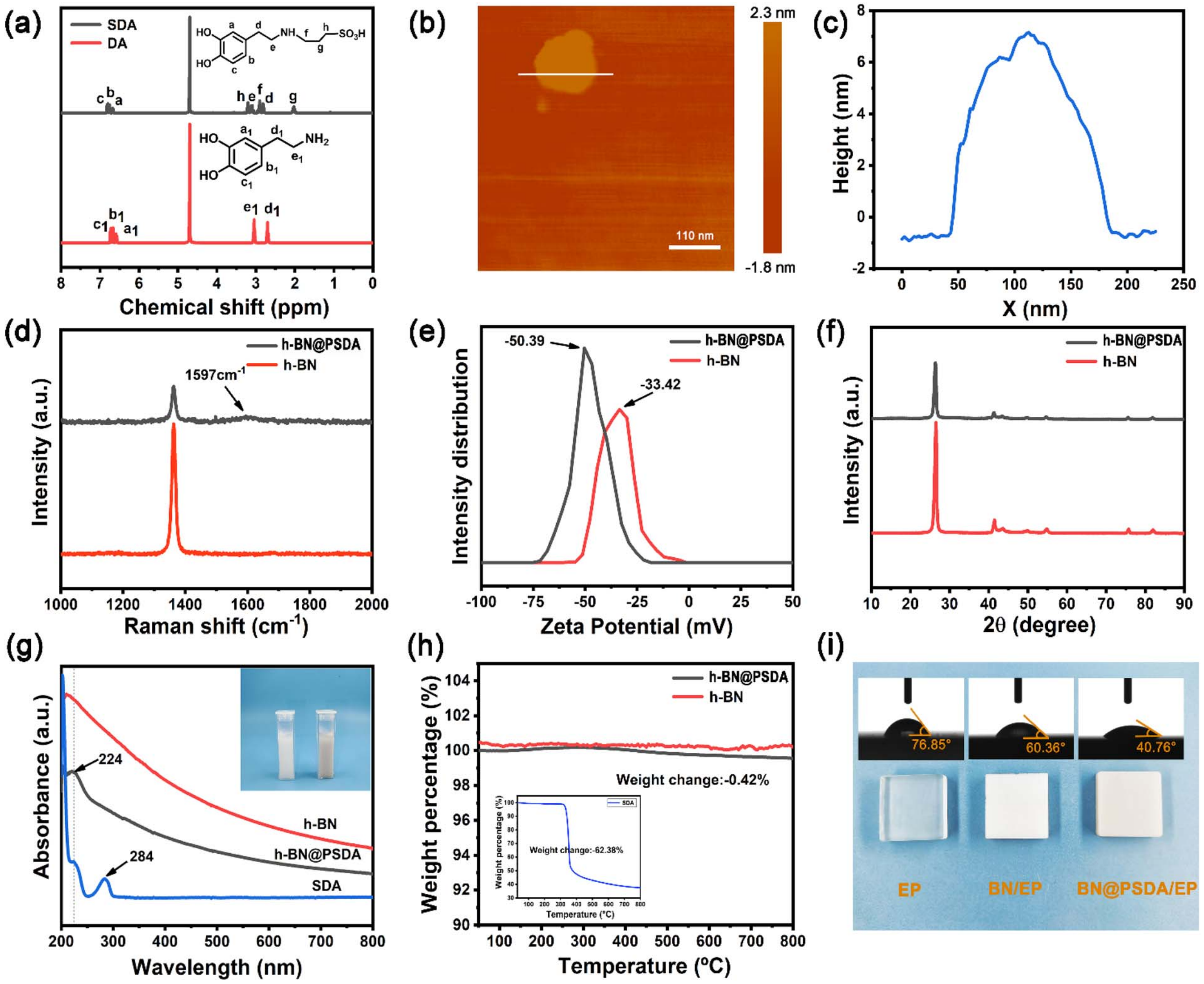

Fig. 3 (a) ^{1}H NMR spectra of DA and SDA. (b) AFM topographic image, and (c) corresponding height profile and size of pristine h-BN nano-sheets. (d) Raman spectra of h-BN and h-BN@PSDA nano-sheets. (e) Zeta potential of h-BN and h-BN@PSDA. (f) XRD patterns of h-BN and h-BN@PSDA. (g) UV-vis absorption spectra and the insets in (g) are images of h-BN and h-BN@PSDA nano-sheet aqueous solutions, respectively. (h) TGA profiles of h-BN and h-BN@PSDA nano-sheets. The insets in (g) are TG images of SDA. (i) Surface morphologies of neat EP, h-BN/EP, and h-BN@PSDA/EP samples, and the corresponding contact angles.

−33.42 mV, whereas the zeta potential of h-BN@PSDA is obviously lower (−50.39 mV), *cf.* Fig. 3e, suggesting that h-BN nano-sheets carry more negative charges after functionalization using PSDA. Fig. 3f shows the XRD spectra of h-BN and h-BN@PSDA. Characteristic peaks at $2\theta = 26.38°$, 41.28°, 43.52°, 49.89°, and 54.87° for both h-BN and h-BN@PSDA were attributed to the (002), (100), (101), (102), and (004) crystal planes of h-BN, respectively, in which (002) and (100) faces are horizontally and vertically aligned crystallization planes. The positions of the peaks for h-BN@PSDA are almost identical to the pristine h-BN, which implies that both the pristine and the modified h-BN are highly crystalline.[41]

Compared to the pristine h-BN, the intensities of the characteristic peaks of h-BN@PSDA are all decreased, indicating that the crystalline faces of h-BN are modified by PSDA. The aqueous h-BN dispersion changes from white to light gray after modification by PSDA, *cf.* inset of Fig. 3g, due to the oxidation of PSDA catechol to quinone. For the pristine h-BN, a peak at 209 nm is observed with the tail extending to the entire visible region, consistent with previous studies.[42] The two characteristic absorption peaks at 224 and 284 nm, respectively, are observed for the PSDA dispersion, as a result of the π–π conversion of the benzene ring unit and the typical absorption of the catechol unit. h-BN@PSDA displays a single characteristic peak at 224 nm owing to the π–π conversion of the benzene ring in PSDA, which indicates the *in situ* spontaneous polymerization of SDA on the h-BN surface.[40] The TGA curves of h-BN nano-sheets before and after PSDA modification are shown in Fig. 3h. The pristine h-BN exhibits ultra-high thermal stability up to 800 °C without any obvious decomposition, whereas pure SDA presents much worse thermal stability with a loss of mass by around 62% at about 315 °C (inset Fig. 3h). For h-BN@PSDA, the mass declines slightly by 0.4% at about 350 °C, *cf.* Fig. 3h, likely due to the thermal degradation of the surface attached PSDA layer. The calculation (percentage mass loss of h-BN@PSDA lost/percentage mass loss of SDA = amount of SDA on h-BN@PSDA) shows that approximately 0.68% of the PSDA is attached to the boron nitride nano-sheets (Fig. 3h). The appearance of the h-BN nano-sheets changes obviously before and after PSDA modification, and the color changes from white to gray, *cf.* Fig. S1a.† Compared to the pristine h-BN, the contact angle of the aqueous h-BN dispersion after PSDA modification decreases greatly from 21° to 12° (Fig. S1b and c†), due to the existence of hydroxyl hydrophilic groups and sulfonic hydrophilic groups on the PSDA.

The hydrophilicity of the h-BN@PSDA reinforced EPs is also significantly improved compared to EPs, with the water contact angle decreasing from 77° to 41°, *cf.* Fig. 3i. The colors of EPs reinforced by different h-BN nano-fillers are also different, which indicates that sulfonated dopamine (SDA) has been successfully functionalized on the h-BN surface.

Fig. 4a–c show the XPS spectra of pristine h-BN and h-BN@PSDA nano-sheets. Both samples are mainly composed of four elements B, N, C and O, respectively. h-BN@PSDA presents a new peak at 167.1 eV, *cf.* Fig. 4c, which belongs to S 2p.[43] The N 1s peak of h-BN@PSDA is divided into three peaks *via* Gaussian curve fitting, corresponding to N–B (398.2 eV), N–C (398.9 eV), and N–H (400.0 eV), respectively, *cf.* Fig. 4b.[21] The h-BN@PSDA with a lattice spacing of 0.217 nm is clearly seen in the HR-TEM image (Fig. 4e), which is consistent with the typical (100) crystal plane of h-BN.[44] In Fig. 4f, EDS elemental mapping of h-BN@PSDA shows that besides the elements O, N, C, and B, a small amount of S element appears on the h-BN surface, which implies that PSDA has been successfully transferred to the h-BN surface. Fig. S2a and b† show the SEM pictures of h-BN nano-sheets before and after PSDA modification. The pristine h-BN nano-sheets are disc-like with clear edges, smooth surfaces and uneven dimensions. The shape of h-BN does not change obviously after PSDA modification.

Fig. 5a shows the thermal conductivity and thermal diffusivity of EPs, h-BN/EPs and h-BN@PSDA/EPs, respectively. The thermal diffusivities of EPs, h-BN/EPs and h-BN@PSDA/EPs are 0.135 mm^2 s^{-1}, 0.142 mm^2 s^{-1}, and 0.147 mm^2 s^{-1}, respectively. The relevant data for density and specific heat capacity needed to calculate the thermal conductivity are shown in Table S1.† The thermal conductivity of the neat EPs is 0.178 W m^{-1} K^{-1} at 25 °C. When adding 0.6 wt% pristine h-BN or h-BN@PSDA in the EP matrix, the thermal conductivity of EPs increased by 4%

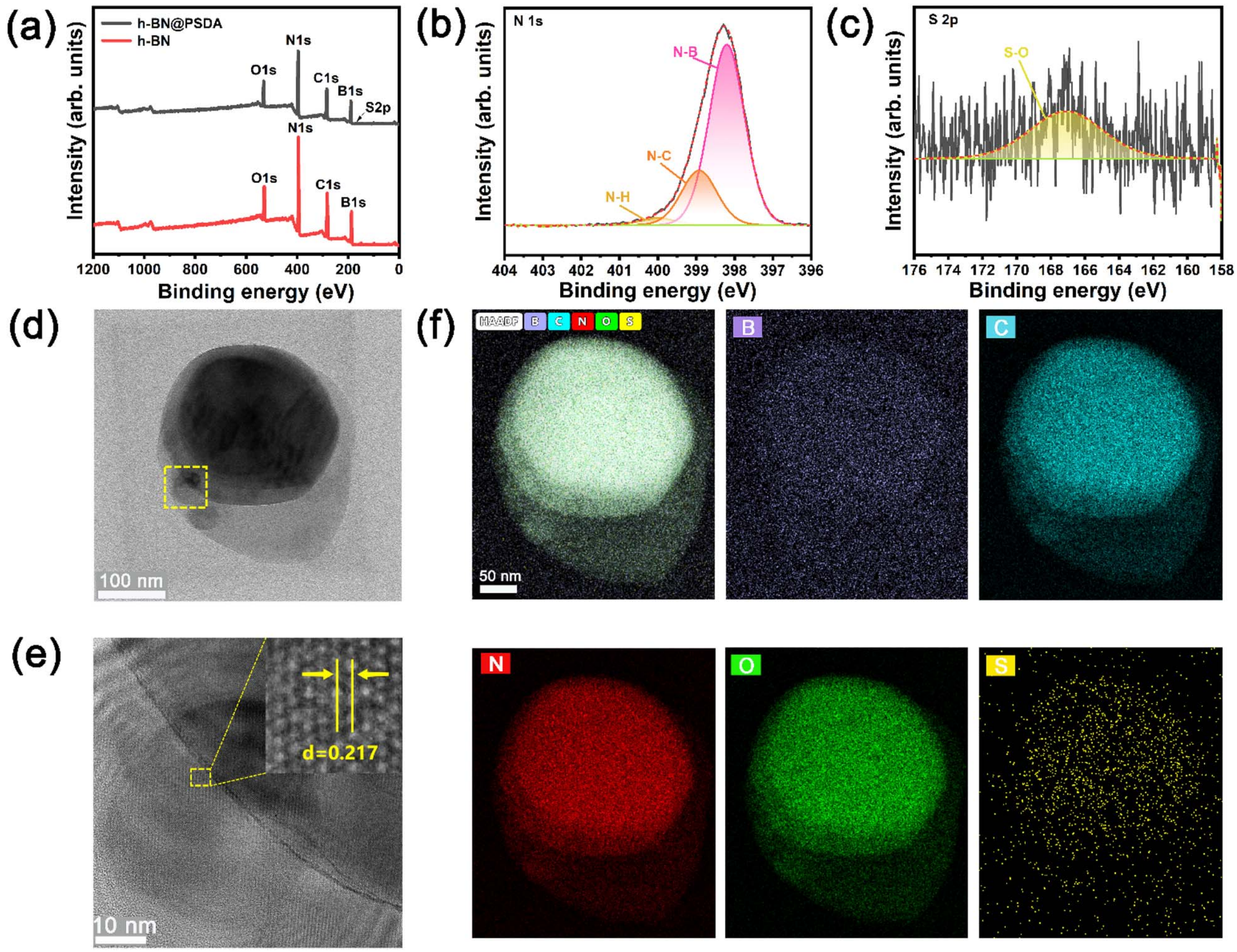

Fig. 4 (a) XPS full spectra of h-BN and h-BN@PSDA. (b) N 1s and (c) S 2p elements of h-BN@PSDA. (d) Low resolution TEM image, (e) HR-TEM image and (f) EDS elemental mapping of h-BN@PSDA, respectively.

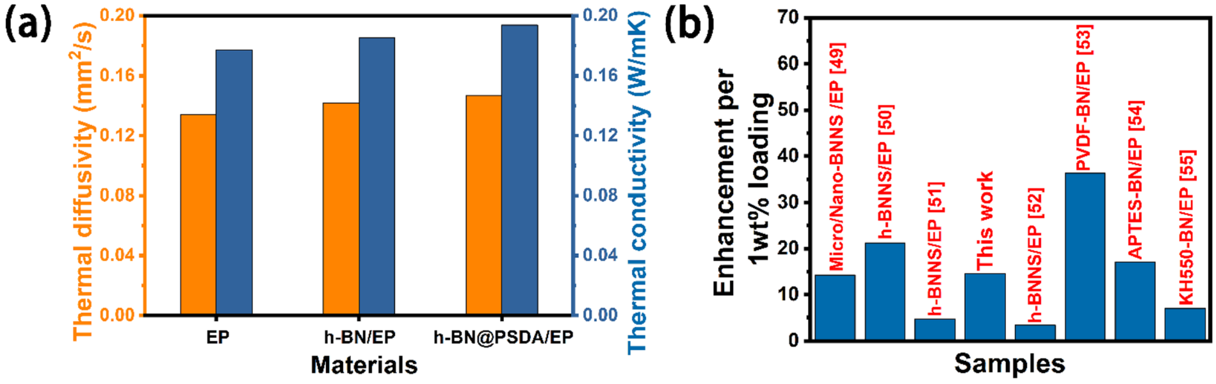

Fig. 5 (a) Thermal diffusivity and thermal conductivities of EPs, h-BN/EPs and h-BN@PSDA/EPs, respectively. (b) Comparison of the enhancement efficiency of the thermal conductivity of the EP composites per 1 wt% h-BN@PSDA fillers.

and 9% to 0.185 and 0.194 W m^{-1} K^{-1}, respectively. h-BN@PSDA performs better than pristine h-BN to improve the thermal conductivity of EPs because they disperse more evenly in the EP matrix due to the increased affinity between PSDA functionalized h-BN and EPs, and thus reduces the phonon scattering at the BN–resin interface and decreases the interfacial thermal resistance. Fig. 5b shows that the h-BN@PSDA/EPs prepared in this work performs at an average level compared to other h-BN/EP composites,[45–51] which means that h-BN@PSDA nano-sheets are promising nano-fillers for improving the thermal and tribological properties of EPs.

Fig. 6a shows the coefficient of friction (COF) curves of EPs, h-BN/EPs and h-BN@PSDA/EPs, respectively, under dry conditions with a short friction test period of 900 s. The COFs of neat EPs and h-BN/EPs increase rapidly during the initial running-in stage (time < 50 s) and then reach the steady state after 100 s. In the steady state, the average COF of h-BN/EPs (0.54) is 14.28% lower than that of neat EPs due to the excellent lubricity of h-BN

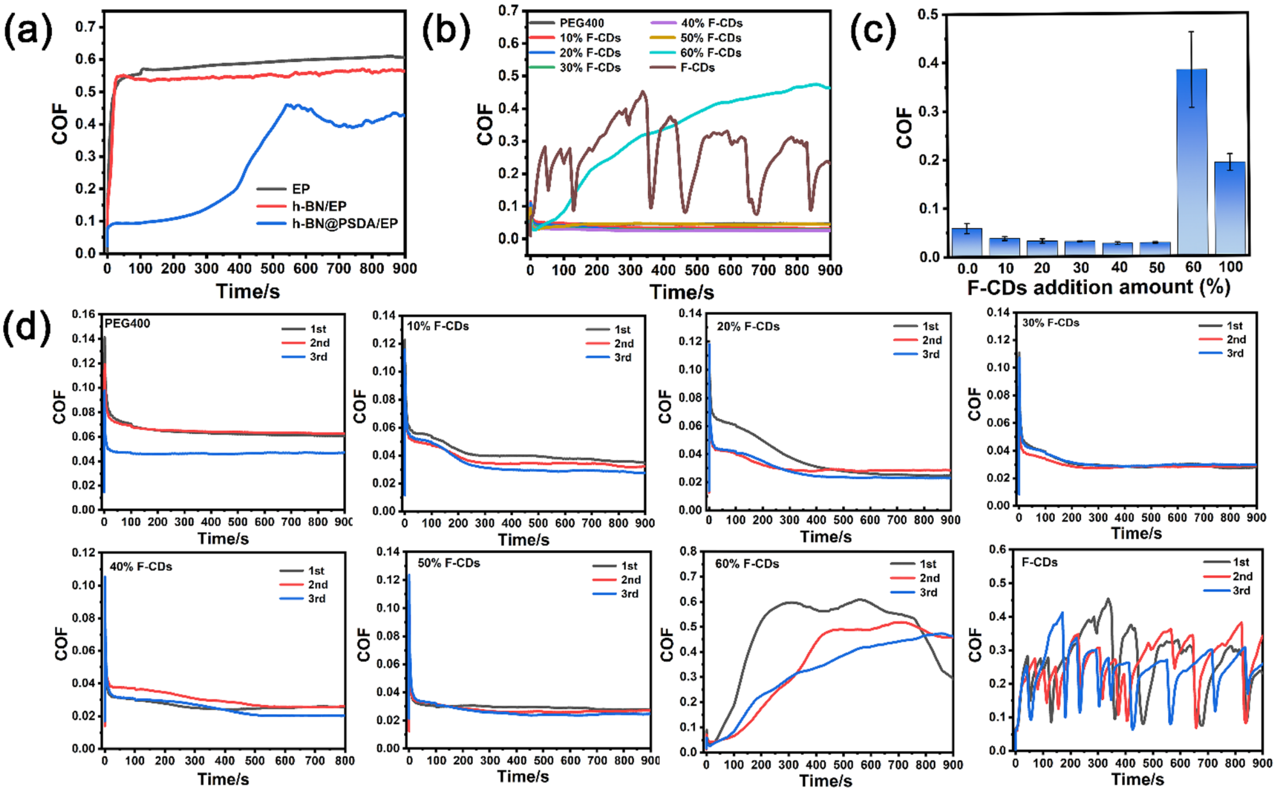

Fig. 6 (a) The coefficient of friction curves of EPs, h-BN/EPs and h-BN@PSDA/EPs, respectively, under dry conditions. (b) The coefficient of friction curves of F-CDs dissolved in PEG 400 at concentrations of 10 wt%, 20 wt%, 30 wt%, 40 wt%, 50 wt%, and 60 wt%, respectively, and (c) the corresponding histograms. (d) The coefficient of friction curves for repeated tests of F-CDs in PEG400 at concentrations of 10 wt%, 20 wt%, 30 wt%, 40 wt%, 50 wt%, and 60 wt%, respectively.

nano-sheets dispersed in h-BN/EPs. h-BN@PSDA/EPs shows a stable and low COF of about 0.18 in the first 300 s, and then it increases gradually to a steady stage with a COF of around 0.45 between 300 s and 900 s, which may be attributed to the destruction of h-BN nanosheets during friction. The average COF of h-BN@PSDA/EPs over the entire 900 s is 0.28, which is 55.56% and 48.15% lower compared with the EPs and h-BN/EPs, respectively. This indicates that h-BN@PSDA nano-sheets possess better lubricity than pristine h-BN in EPs.

To further improve the tribological properties of epoxy composites, a bioinspired solvent-free carbon dot (F-CD)-based nanofluid is introduced for the first time as the lubricant for the steel-EP counter bodies. The COFs of pure PEG400, pure F-CDs and F-CDs dispersed in PEG 400 at concentrations of 10 wt%, 20 wt%, 30 wt%, 40 wt%, 50 wt%, and 60 wt%, respectively for a friction test period of 900 s are shown in Fig. 6b and c, the repeated results are shown in Fig. 6d. The COF curve of pure PEG 400 is smooth with an average value of 0.056, which means it is a good lubricant for the steel–EP system. Despite significant fluctuation, the COF curve of pure F-CDs shows an average value of 0.25, which is still obviously lower than under the dry condition and suggests the positive effect of F-CDs on friction reduction. For the F-CDs dispersed in PEG 400, the lowest and most stable COF curve with an average value of 0.028 is achieved at an F-CD concentration of 40 wt% for a friction test period of 900 s, which is even 50.00% lower than that of pure PEG 400. The COF becomes worse when the dosage of F-CDs exceeds 40 wt%, indicating the appearance of severe abrasive wear triggered by the aggregation of excessive F-CD nanoparticles. These results indicate that an appreciable beneficial synergistic effect is achieved on the EP surface when using F-CDs/PEG 400 mixtures as the lubricants.

In order to further study the long-term performances of the systems, friction tests up to 7200 s were conducted, *cf.* Fig. 7. Without lubricants, the h-BN@PSDA/EPs shows higher friction than EPs when the friction test is longer than 3500 s (Fig. 7a), which may be caused by the accumulation of wear debris in the contact region. The COF of h-BN@PSDA/EPs lubricated by pure PEG 400 decreases gradually and reaches the stable state of 0.073 at around 300 s, in line with the short-term tests in Fig. 6 and means that PEG 400 lubricates the h-BN@PSDA/EP system very well (Fig. S3a†). The addition of 40 wt% F-CDs in PEG 400 further reduces the COF of the h-BN@PSDA/EP system by 56.16%, *cf.* Fig. 7a and b.

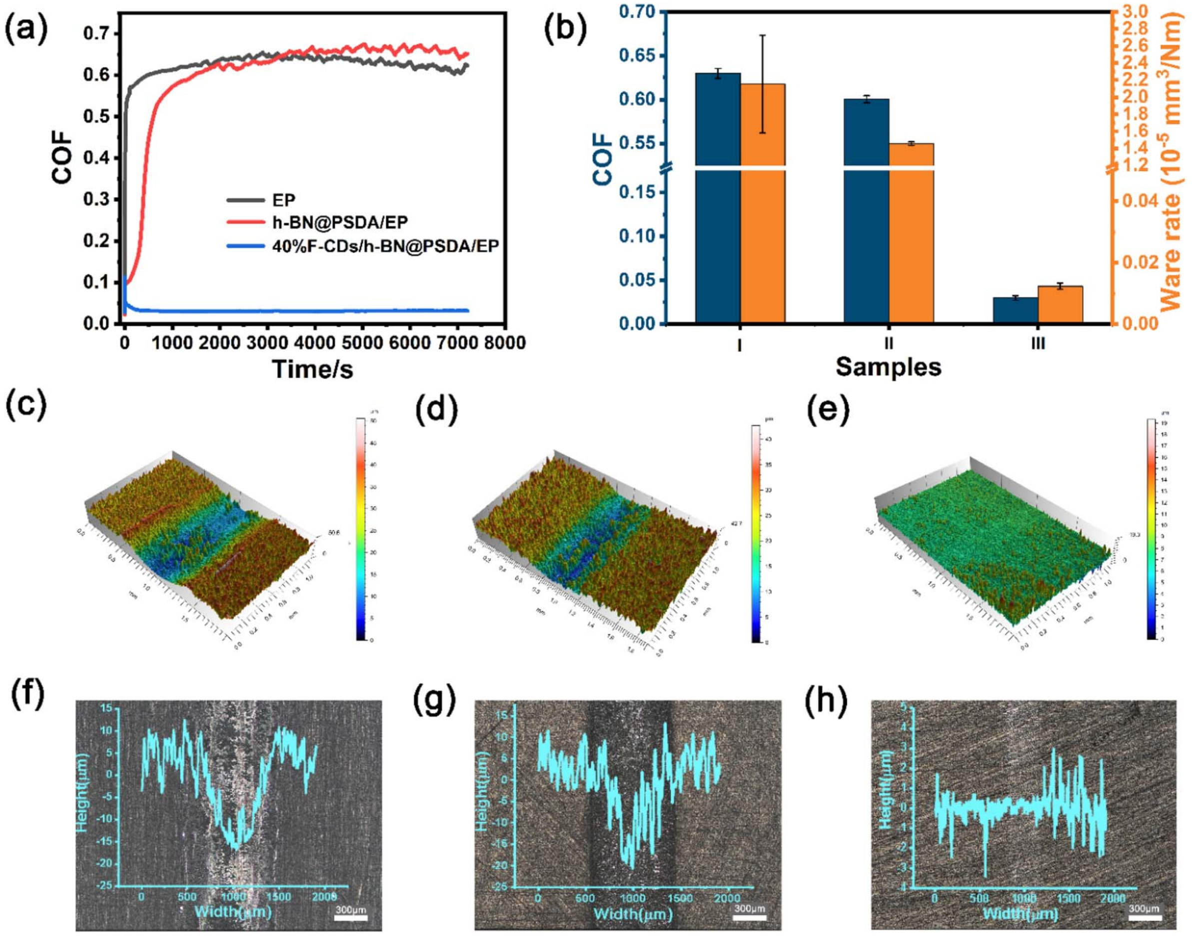

Fig. 7 (a) The coefficient of friction curves and (b) the average coefficient of friction and wear rate of EPs (I), h-BN@PSDA/EPs (II), F-CDs/h-BN@PSDA/EPs (III) obtained from a long friction test of 7200 s. (c–e) 3D cross-sectional profiles and laser confocal microscopy images; (f–h) corresponding worn surfaces for EPs (c and f) and h-BN@PSDA/EPs (d and g), 40 wt% F-CDs/h-BN@PSDA/EPs (e and h), respectively.

Fig. 7c–h present the 3D morphologies and optical images of the worn surfaces. Clearly, neat EP displays the largest wear width and depth. With the addition of h-BN@PSDA, the wear of h-BN@PSDA/EPs was significantly reduced and the wear track became narrower and shallow, which confirmed that the presence of h-BN nanosheets increased the wear resistance. Significantly smoother surfaces with negligible grooving are detected for h-BN@PSDA/EPs lubricated by pure PEG 400 (Fig. S3c†) and 40 wt% F-CDs in PEG 400, respectively, meaning that these two liquids are excellent lubricants for the h-BN@PSDA/EP system. The optical images of the wear tracks are consistent with the 3D morphologies and show that F-CDs/h-BN@PSDA/EPs has narrower width and lighter depth than wear tracks for other systems. The wear rates calculated from the 3D morphologies are plotted in Fig. 7b. Compared to neat EP, the wear rate of h-BN@PSDA/EPs decreases by 32.48%, *cf.* Fig. 7b, likely due to less severe wear in the initial wear-in period. The wear rate of h-BN@PSDA/EPs lubricated by 40 wt% F-CD dispersion in PEG 400 is 99.42% lower than neat EPs under dry conditions and 22.26% lower than h-BN@PSDA/EPs lubricated by pure PEG 400, respectively. The abrasion rate trend is consistent with the COF trend, confirming that the optimum lubricating system is 40 wt% F-CDs/PEG 400 even in long-term friction tests.

Fig. 8a shows the Raman spectra of the worn surfaces of neat EPs and h-BN@PSDA/EPs under dry conditions and h-BN@PSDA/EPs lubricated by 40 wt% F-CDs in PEG 400. For neat EPs under dry conditions, the characteristic peaks obtained in the worn area are the same as those obtained in the non-worn area, suggesting that no tribo-film was formed to aid lubrication during the friction test. Compared to neat EPs, the characteristic Raman peak of h-BN (1364 cm^{-1}) is observed in the worn area of the h-BN@PSDA/EPs under dry conditions. This result confirms that a lubricating film containing h-BN nano-sheets derived from h-BN@PSDA forms in the contact region to resist wear. For the wear surface of h-BN@PSDA/EPs lubricated in PEG 400, the characteristic peak from h-BN is observed at 1364 cm^{-1} at the wear trace (Fig. S4†). For the worn surface of h-BN@PSDA/EPs lubricated by 40 wt% F-CDs in PEG 400, the characteristic peak of h-BN is still observed in the worn area. This demonstrates that h-BN@PSDA plays a vital role in the friction process even in the presence of a lubricant and works in concert with nanosized F-CDs to form an effective lubricating film. The morphology of the worn surface was measured using SEM and confocal optical microscopy, *cf.* (Fig. 8b, d and S5†), respectively. The wear widths of EPs, h-BN@PSDA/EPs, PEG 400/h-BN@PSDA/EPs and F-CDs/h-BN@PSDA/EPs are 0.86, 0.79, 0.32 and 0.25 mm, respectively (Fig. S5†). For dry neat EPs in Fig. 8b, obvious micro-cracking is observed along with grooves and delamination, likely because neat EP is very brittle, leading to severe adhesive wear. The worn

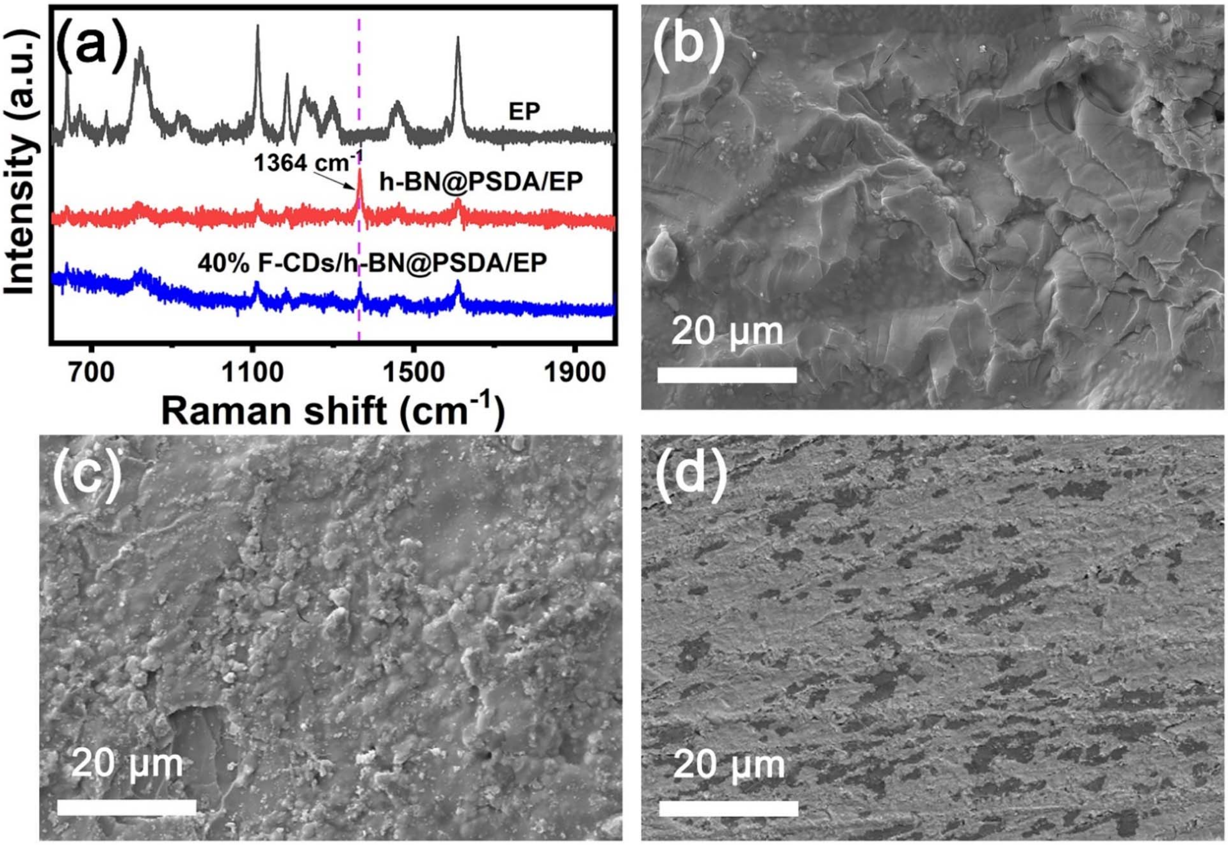

Fig. 8 (a) Raman spectra and SEM images of the worn surfaces of (b) neat EPs, (c) h-BN@PSDA/EPs, (d) 40 wt% F-CDs/h-BN@PSDA/EPs, respectively.

surface of the h-BN@PSDA/EPs without lubrication is smoother and flatter than that of neat EPs (Fig. 8c), which is attributed to the good dispersion of h-BN@PSDA nanosheets in the EP matrix, thus preventing crack extension in the EP matrix by means of a spatial barrier.[52] For the F-CDs/h-BN@PSDA/EPs, the application of 40 wt% F-CDs/PEG 400 as the lubricant leads to a shallower and narrower wear track, which confirms that the addition of fluid-like carbon dots has an obviously positive effect on the wear reduction (Fig. 8d).

Fig. 9 shows TEM images of the fluid lubricant residue of F-CDs/h-BN@PSDA/EPs on the worn surface. Abrasive wear debris produced during the friction test assembles into complicated nano-structures composed of h-BN nano-sheets and F-CDs, *cf.* Fig. 9b. A lattice spacing of 0.34 nm, detected from the selected areas marked in green, is typical of the (002) crystal plane of h-BN;[12,53] a smaller lattice spacing of 0.23 nm (marked in yellow) is also identified, which is consistent with the (100) crystal plane of graphitic carbon.[34] The EDS elemental mapping of Fig. 9c shows that the nanostructure is composed of five elements B, C, N, O and S, respectively, and these five elements are distributed almost evenly across the nanostructure, implying that the F-CDs and h-BN nano-sheets are hybridized together.[54] Fig. 9d shows the cross-sectional TEM image of the tribo-film formed on the worn counter surface (the steel ball) for h-BN@PSDA/EPs lubricated by 40 wt% F-CDs in PEG 400. A thick tribo-film of around 100 nm was formed. The EDS elemental maps in

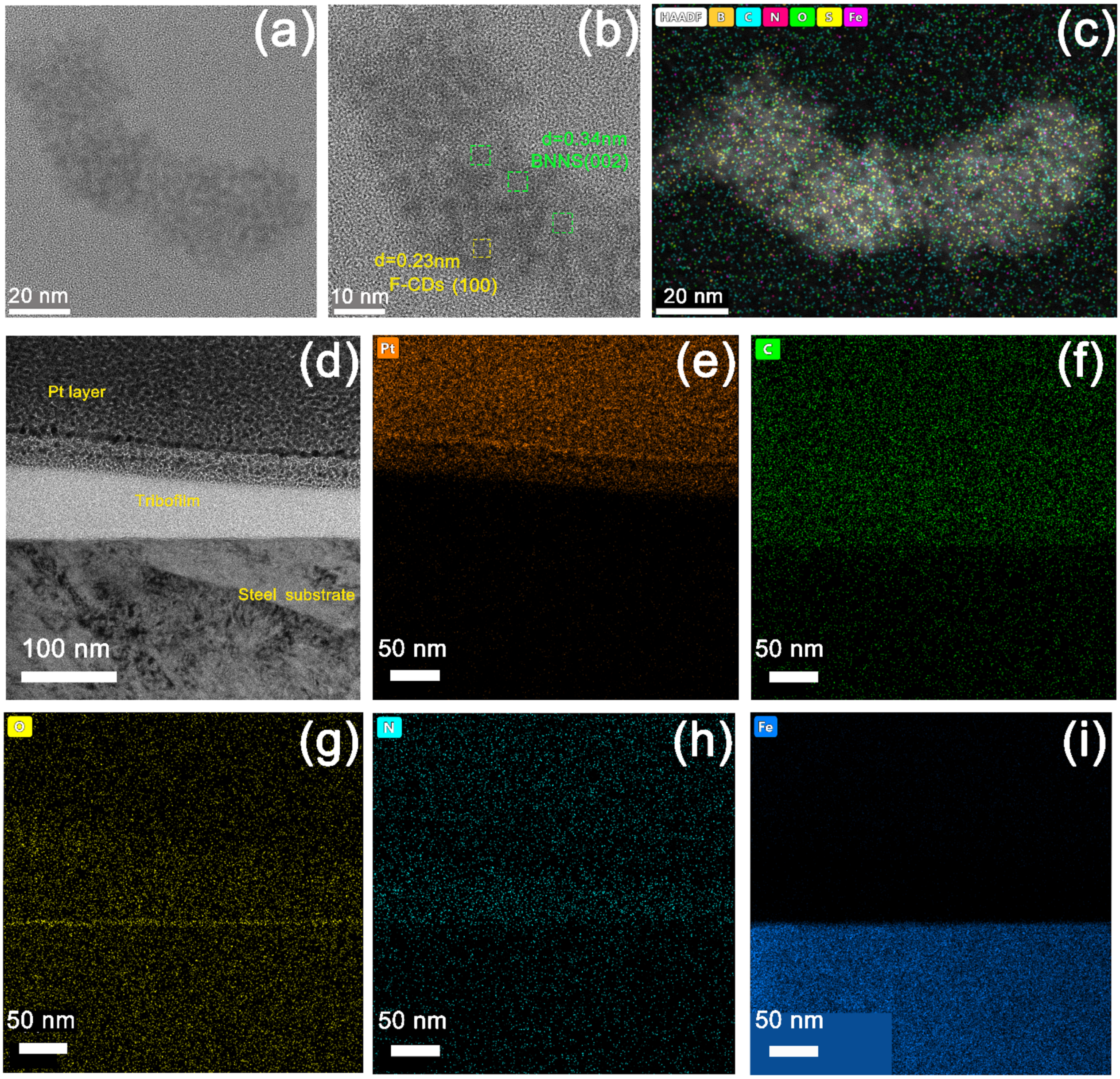

Fig. 9 (a and b) TEM images of the fluid lubricant residue of F-CDs/h-BN@PSDA/EPs on the worn surface. (c) EDS elemental maps for the TEM image of (a). (d) Cross-sectional TEM image of a selected position of the worn counter surface (steel ball), and (e–i) the corresponding EDS elemental maps of Pt, C, N, O and Fe.

Fig. 9e–i reveal that the worn surface is predominantly composed of C, Fe, N and O. A continuous iron oxide layer is observed underneath the tribo-film. This indicates that the frictional oxidation of the steel surface occurs through direct friction of the sliding pairs before the protective friction film grows. In contrast, the tribo-film above the iron oxide layer is mainly composed of C, N and O elements, which are mainly derived from the abrasive debris of the EP matrix during the friction process.

Fig. 10 shows the XPS spectra of B 1s, N 1s, S 2p, C 1s, O 1s, and Fe 2p obtained on the worn steel counter surfaces for h-BN@PSDA/EPs lubricated by pure PEG 400 and 40 wt% F-CDs in PEG 400, respectively.[55] The XPS spectra of the worn counter steel surfaces sliding against EPs and h-BN@PSDA/EPs under dry conditions are shown in Fig. S6.† For h-BN@PSDA/EPs both lubricated with and without F-CDs, the binding energy of N 1s (Fig. 10b) is located at 400.0 eV, which is attributed to the N–C of organic nitrogen compounds. The binding energy peak of N at 398.6 eV for h-BN@PSDA/EPs lubricated by 40 wt% F-CDs in PEG 400 is due to the cationic structure of the N of the F-CDs which can be further confirmed in Fig. 9b. This indicates that the anions of F-CDs are partially transferred to the surface of the steel balls due to electrostatic adsorption. In Fig. 10c, the high-resolution S 2p spectrum is divided into two peaks, where the peaks are separated from each other by about 1.16 eV, with an area ratio of 1 : 2. The metal sulfates could be observed on the lubricated film on the steel ball surface based on the S $2p_{3/2}$ peak at 168.0 eV.[41] In addition, Fig. 10a shows that the peak of the B–O bond can be observed in the fine spectrum of B, which corresponds to the peak of B–O in the O 1s spectrum (Fig. 10e), confirming that the boron oxides were generated in the tribo-film by the slight oxidation of h-BN due to the frictional heat generation and accumulation in the tribo-chemical reaction.[19] Compared to the B 1s spectrum of PEG 400, boron oxides were detected only in the friction film under 40 wt% F-CD lubrication, indicating that h-BN is transferred to the surface of the counter ball with the help of carbon dots. The products generated by the tribo-chemical reaction together form a protective friction film, thus avoiding the direct contact between the steel ball and the resin matrix, and the wear of the resin matrix is reduced.

For h-BN@PSDA/EPs lubricated by pure PEG 400, in Fig. 10f, the Fe 2p spectrum is divided into two doublets, where peaks in each doublet are separated by approximately 13.6 eV, with an area ratio of 1 : 2. The Fe $2p_{3/2}$ peaks at 706.7 eV, 709.6 eV and 710.9 eV indicated that the major existing species of Fe on the worn surface are Fe metal, FeO and Fe_2O_3, respectively.[56] The peak at 529.5 eV in O 1s confirms the formation of iron oxide, which means that the serious oxidation of the iron substrate (steel ball) is caused by the heat generated in the friction process increasing the local temperature of the contact area. The deconvoluted C 1s peaks at 288.9 eV, 287.9 eV, 286.4 eV and 284.8 eV are assigned to O–C=O, C=O, C–O/C–N and C–C groups originating from the EP matrix, which are confirmed by the O 1s peaks at 533.1 eV, 532.3 eV and 531.0 eV.[57]

For h-BN@PSDA/EPs lubricated by 40 wt% F-CDs in PEG 400, the binding energy of Fe 2p is divided into a doublet, where doublet peaks are separated by approximately 13.6 eV, with an area ratio of 1 : 2. The deconvoluted Fe $2p_{3/2}$ peaks is located at 709.6 eV and 714.1 eV, which indicates that the formed tribo-film on the worn steel surface consists of FeO.[36] Furthermore, the deconvoluted C 1s spectrum shows a metal carbide peak at 283.6 eV, which may be attributed to the tribo-chemical reaction between carbon dots and iron matrix during friction, with other components corresponding to C–C, C–O/C–N, C=O and O–C=O bonds. The O 1s peaks located at 529.5 eV, 531.0 eV, 532.3 eV, and 534.4 eV correspond to Fe–O, C–O, C–OH and B–O.

In summary, organic nitrogen compounds, boron oxides, iron oxides, metal carbides and iron sulfides consist of the tribo-film on the counter steel ball. These tribo-chemical

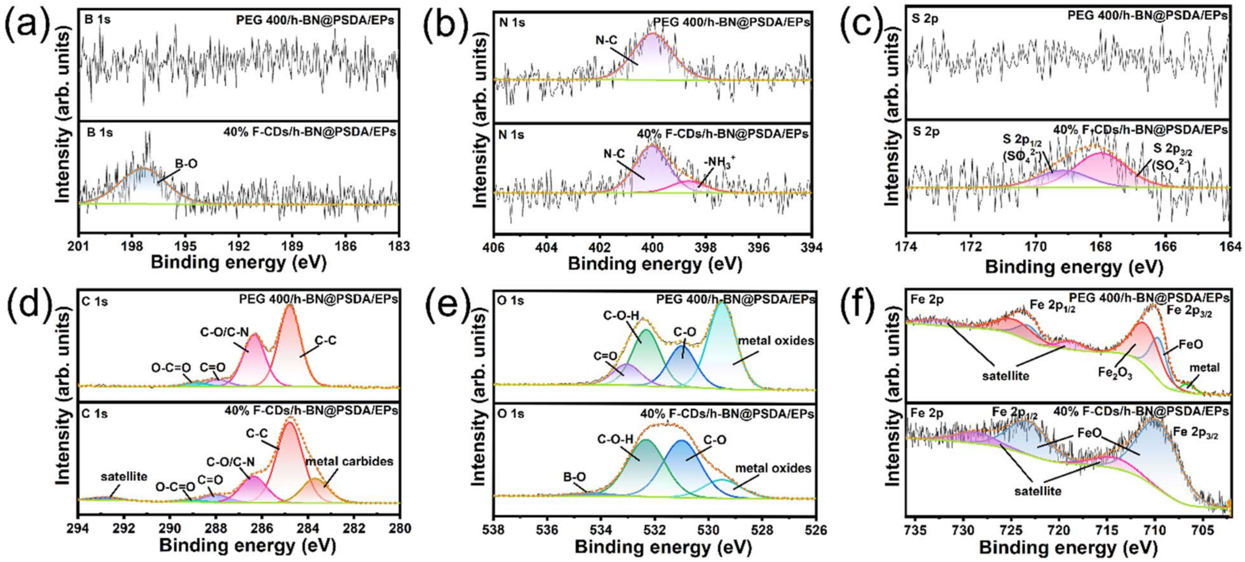

Fig. 10 (a–f) XPS spectra of the tribo-film formed on the worn counter surface (steel ball) for h-BN@PSDA/EPs lubricated by pure PEG 400 and 40 wt% F-CDs in PEG 400.

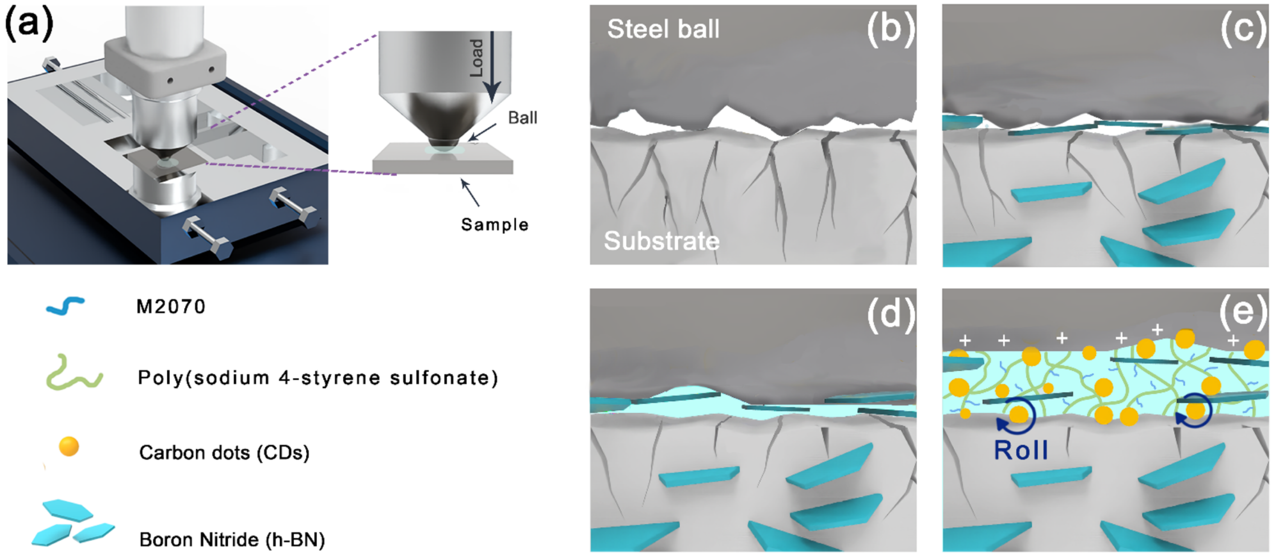

Fig. 11 (a) Schematic of the lubrication mechanism for h-BN@PSDA/EPs lubricated by 40 wt% F-CDs in PEG 400. Schematic of the lubrication mechanism of (b) EP, (c) h-BN@PSDA/EPs, (d) h-BN@PSDA/EPs lubricated by PEG 400, (e) h-BN@PSDA/EPs lubricated by 40 wt% F-CDs in PEG 400.

reaction products effectively prevented the direct contact of the EP substrate with the steel substrate, which further improved the tribological properties of EPs.

According to the characterization results above, the lubrication mechanisms of neat EPs under dry conditions, and h-BN@PSDA/EPs under dry conditions as well as those lubricated by F-CDs in PEG 400 are proposed as follows. The EP matrix is easily transferred and adsorbed on the steel surface owing to the shearing force and the strong van der Waals interaction, thus forming a dense EP lubricating film on the iron substrate.[58] Neat EP is brittle and has low thermal conductivity, leading to long microcracks and severe wear during friction tests. The negatively charged sulfonic acid group on the interface of h-BN@PSDA enhances the electronegativity of h-BN nanosheets. The weaker the interaction force between the boron nitride nanosheets, the better the dispersion stability in the matrix. Due to the improved dispersivity and interfacial adsorption of h-BN@PSDA nano-sheets in the resin matrix, the load-bearing capacity of h-BN@PSDA/EPs is enhanced, hence the expansion of microcracks is effectively inhibited, and the tribological performance is improved under dry conditions.[59,60]

Meanwhile, the h-BN nanosheets derived from the h-BN@PSDA/EP matrix will form a tribofilm in the contact area between the positively charged steel balls and EPs by the electrostatic interaction between the charges protecting the brittle EP matrix from further wear against hard steel balls. The inevitable accumulation and agglomeration of abrasive debris makes it difficult to provide sufficient h-BN@PSDA nanosheets to maintain a strong friction film during frictional operation, and thus unavoidable frictional failure occurs, eventually leading to the sharp increase of COF, *cf.* Fig. 7a. This problem is further improved by introducing fluid lubricants, F-CDs in PEG 400 in this study, *cf.* Fig. 11. The three-dimensional polymer network introduced on the surface of carbon dots creates a flexible layer on the surface of the carbon dots, which would reduce the damage to carbon dots and protect the resin matrix from abrasion by the nanoparticles.[61] During the friction process, the multiple adsorption sites in the polymer network can drive the uniform fixation of the carbon dots on the steel ball surface, while the charged F-CDs adsorbed to the micro-concave on the steel surface, thereby promoting the formation of an electric double layer at the contact surface.[62,63] This leads to the rapid formation of a stable and strong friction film at the friction interface. The flexible polymer network further ensures a stable coefficient of friction. The polyethylene glycol 400 base oil mainly acts as a nano additive carrier here. Meanwhile, the h-BN@PSDA and F-CD carbon dot ionic fluids exfoliated from the resin matrix during the reciprocal friction motion are assembled into nano-hybrid nanostructures induced by electrostatic adsorption, which exhibit a “rolling–sliding” effect and a “self-repairing” effect by filling the deep scratches on both surfaces.[37,65,66] Furthermore, during the reciprocal sliding, the products generated by the tribo-chemical reactions form a continuous protective layer on the surface of the steel ball, which can well avoid direct contact between the friction pairs, thus playing a role in reducing friction.[64]

Conclusions

In this work, inspired by the lubricating mechanism and structure of natural snail mucus, we have successfully designed a high-performance lubricating system for EPs. Firstly, improved interfacial compatibility and dispersion of the h-BN@PSDA nanosheets with the epoxy resin matrix have been provided by the negatively charged groups of PSDA functionalized on the h-BN surface. Then, a bio-inspired solvent-free carbon dot-based (F-CDs) nanofluid with a three-dimensional and multiple adsorption polymer network structure has been prepared and shown promising performances when used as lubricants for EPs. The F-CDs are immobilized on the contact areas and form a stable, strong and durable lubricating film owing to the multiple adsorption effects and branching structures. A positive tribological synergy of h-BN@PSDA reinforced epoxy composites with the bioinspired F-CDs leads to a significant reduction in friction by 95.25% and wear by 99.42% of the epoxy resin after long-term sliding. The added F-CD nanofluid triggers the "rolling sliding" and "self-repair" effects by filling deep scratches on both contact surfaces. Meanwhile, h-BN@PSDA nano-fillers and the F-CD nanofluid form a hybrid nanostructure during sliding due to the electrostatic attraction, resulting in an effective improvement of the tribological properties of EP. The outcomes will shed light on the development of advanced carbon dot-based nanofluid lubricants for nano-filler reinforced composites and a wide range of other applications in the future.

Author contributions

Chengcheng Jiao: methodology, formal analysis, investigation, writing – original draft, writing – review & editing. Tao Cai: conceptualization, supervision, investigation, project administration, writing – review & editing, funding acquisition. Huanyi Chen: methodology, formal analysis, investigation. Xinxin Ruan: methodology, formal analysis, investigation. Yandong Wang: writing review. Ping Gong: writing review. Hua Li: supervision, writing review & editing. Rob Atkin: supervision, writing review & editing. Feng Yang: supervision, investigation; Nishimura: supervision; Haichao Zhao: Jinhong Yu: supervision, investigation; Nan Jiang: supervision, investigation.

Conflicts of interest

The authors declare that they have no known competing financial interests or personal relationships that could have appeared to influence the work reported in this paper.

Acknowledgements

We sincerely appreciate the financial supports from the National Natural Science Foundation of China (52075527, 51573201), National Key R&D Program of China (2017YFB0406000 and 2017YFE0128600) and the Natural Science Foundation of Ningbo (2019A610028), the Project of the Chinese Academy of Science (ZDKYYQ20200001), Ningbo 3315 Innovation Team (2019A-18-C).

References

1 H. Liang, M. Xu, X. Chen, Y. Bu, Y. Zhang, K. Gao, C. Min, X. Hua and Y. Fu, *Wear*, 2021, **486–487**, 204109.
2 Q. Zhao, Z. Lu, Y. Wu and W. Zhao, *Compos. Sci. Technol.*, 2022, **217**, 109090.
3 M. S. Goyat, A. Hooda, T. K. Gupta, K. Kumar, S. Halder, P. K. Ghosh and B. S. Dehiya, *Ceram. Int.*, 2021, **47**(16), 22316–22344.
4 Y. Zhang, X. He, M. Cao, X. Shen, Y. Yang, J. Yi, J. Guan, J. Shen, M. Xi, Y. Zhang and B. Tang, *Materials*, 2021, **14**(10), 2509.
5 Z. Zhang, Y. Du, C. Zhu, L. Guo, Y. Lu, J. Yu, I. P. Parkin, J. Zhao and D. Guo, *Nanoscale*, 2021, **13**(5), 2855–2867.
6 S. Li, J. Zhang, M. Liu, R. Wang and L. Wu, *Polym. Bull.*, 2020, **78**(11), 6493–6515.
7 F. Meng, Z. Zhang, P. Gao, R. Kang, Y. Boyjoo, J. Yu and T. Liu, *Friction*, 2020, **9**(4), 734–746.
8 C. Liu, M. Li, Q. Shen and H. Chen, *Materials*, 2021, **14**(7), 1731.
9 B. Chen, Y. Jia, M. Zhang, H. Liang, X. Li, J. Yang, F. Yan and C. Li, *Composites, Part A*, 2019, **122**, 85–95.
10 Y. Du, Z. Zhang, D. Wang, L. Zhang, J. Cui, Y. Chen, M. Wu, R. Kang, Y. Lu, J. Yu and N. Jiang, *Friction*, 2021, **10**(6), 854–865.
11 B. Chen, M. Zhang, X. Li, Z. Dong, Y. Jia and C. Li, *Prog. Org. Coat.*, 2020, **147**, 105767.
12 L. An, Y. Yu, C. Bai, Y. Bai, B. Zhang, K. Gao, X. Wang, Z. Lai and J. Zhang, *npj 2D Mater. Appl.*, 2019, **3**(1), 28.
13 H. Huang, X. Huang, Y. Xie, Y. Tian, X. Jiang and X. Zhang, *Prog. Org. Coat.*, 2019, **130**, 124–131.
14 H. Zhang, X. Zhang, K. Zheng and X. Tian, *RSC Adv.*, 2021, **11**(36), 22343–22351.
15 S. S. Pasare and B. Suresha, *AIP Conf. Proc.*, 2020, **2236**, 040005.
16 M. G. Rasul, A. Kiziltas, M. S. Bin Hoque, A. Banik, P. E. Hopkins, K.-T. Tan, B. Arfaei and R. Shahbazian-Yassar, *Tribol. Int.*, 2022, **165**, 107277.
17 J. Song, Z. Dai, J. Li, H. Zhao and L. Wang, *Polym.*, 2017, **31**(1), 116–123.
18 B. Chen, Z. Dong, J. Li, M. Zhang and K. Zhang, *Prog. Org. Coat.*, 2021, **161**, 106493.
19 G. Li, Y. Ma, H. Xu, L. Chen, Y. An, M. Gao, H. Zhou and J. Chen, *Prog. Org. Coat.*, 2022, **165**, 106731.
20 W. Zhao, W. Zhao, Z. Huang, G. Liu and B. Wu, *Chem. Phys. Lett.*, 2019, **732**, 136646.
21 Z. Zhang, H. Yuan, F. Qi, N. Zhao, B. Zhang and X. Ouyang, *Ind. Eng. Chem. Res.*, 2021, **60**(23), 8430–8441.
22 S. E, X. Ye, M. Wang, J. Huang, Q. Ma, Z. Jin, D. Ning and Z. Lu, *Appl. Surf. Sci.*, 2020, **529**, 147054.
23 Y. He, H. Li, C. Qu, W. Cao and M. Ma, *Green Chemical Engineering*, 2021, **2**(2), 145–157.
24 B. Bhattacharjee, P. Chakraborti and K. Choudhuri, *Tribol. Int.*, 2019, **138**, 415–423.
25 G. Huang, Q. Yu, Z. Ma, M. Cai, F. Zhou and W. Liu, *Friction*, 2017, **7**(1), 18–31.
26 J. Song, *ACS Omega*, 2021, **6**(44), 29345–29349.
27 J. M. Liñeira del Río, E. R. López and J. Fernández, *J. Mol. Liq.*, 2020, **301**, 112442.
28 Z. Zheng, X. Liu, H. Yu, H. Chen, D. Feng and D. Qiao, *Friction*, 2022, **10**(12), 2000–2017.
29 K. I. Nasser, J. M. Liñeira del Río, F. Mariño, E. R. López and J. Fernández, *Tribol. Int.*, 2021, **163**, 107189.
30 F. Zhao, L. Zhang, G. Li, Y. Guo, H. Qi and G. Zhang, *Carbon*, 2018, **136**, 309–319.

31 W. Tang, Z. Zhang and Y. Li, *J. Mater. Sci.*, 2021, **56**(21), 12061–12092.

32 W. Shang, T. Cai, Y. Zhang, D. Liu and S. Liu, *Tribol. Int.*, 2018, **118**, 373–380.

33 M. Ye, T. Cai, L. Zhao, D. Liu and S. Liu, *Tribol. Int.*, 2019, **136**, 349–359.

34 Z. Mou, B. Wang, H. Lu, S. Dai and Z. Huang, *Carbon*, 2019, **154**, 301–312.

35 H. Xiao, S. Liu, Q. Xu and H. Zhang, *Sci. China: Technol. Sci.*, 2018, **62**(4), 587–596.

36 L. Zhao, T. Cai, M. Ye, D. Liu and S. Liu, The regulation of the microstructure, *Carbon*, 2019, **150**, 319–333.

37 C. Liu, Q. Yin, W. Zhang, Y. Bao, P. Li, L. Hao and J. Ma, *Carbon*, 2021, **183**, 504–514.

38 Z. Mou, Q. Yang, B. Zhao, X. Li, Y. Xu, T. Gao, H. Zheng, K. Zhou and D. Xiao, *ACS Sustainable Chem. Eng.*, 2021, **9**(44), 14997–15007.

39 H. Ruan, Z. Zheng, J. Pan, C. Gao, B. Van der Bruggen and J. Shen, *J. Membr. Sci.*, 2018, **550**, 427–435.

40 C. Bai, F. Wang, Z. Zhao, B. Zhang, Y. Yu and J. Zhang, *Mater. Today Nano*, 2021, **15**, 100129.

41 X. Zhang, J. Yi, Y. Yin, Y. Song and C. Xiong, *Diamond Relat. Mater.*, 2021, **117**, 108485.

42 B. Singh, G. Kaur, P. Singh, K. Singh, B. Kumar, A. Vij, M. Kumar, R. Bala, R. Meena, A. Singh, A. Thakur and A. Kumar, *Sci. Rep.*, 2016, **6**, 35535.

43 J. Ding, H. Wu and P. Wu, *J. Membr. Sci.*, 2020, **598**, 117658.

44 C. Bai, L. An, J. Zhang, X. Zhang, B. Zhang, L. Qiang, Y. Yu and J. Zhang, *Chem. Eng. J.*, 2020, **402**, 126206.

45 C. Zhang, J. Xiang, S. Wang, Z. Yan, Z. Cheng, H. Fu and J. Li, *Materials*, 2021, **14**(13), 3521.

46 I. Isarn, F. Ferrando, À. Serra and C. Urbina, *Polym. Adv. Technol.*, 2020, **32**(4), 1485–1492.

47 C. e. Yue, L. Guan, X. Zhang, Y. Wang and L. Weng, *Mater. Des.*, 2021, **212**, 110190.

48 L. Guo, S. Ding, S. Yuan, X. Gou, F. Cai, D. Wang and H. Zhao, *e-Polymers*, 2021, **21**(1), 681–690.

49 X. Chen, J. S. K. Lim, W. Yan, F. Guo, Y. N. Liang, H. Chen, A. Lambourne and X. Hu, *ACS Appl. Mater. Interfaces*, 2020, **12**(14), 16987–16996.

50 J. Hou, G. Li, N. Yang, L. Qin, M. E. Grami, Q. Zhang, N. Wang and X. Qu, *RSC Adv.*, 2014, **4**(83), 44282–44290.

51 J. Gu, Q. Zhang, J. Dang and C. Xie, *Polym. Adv. Technol.*, 2012, **23**(6), 1025–1028.

52 Y. Zhou, M. Liu, Y. Wang, J. Yuan and X. Men, *Tribol. Int.*, 2022, **165**, 107328.

53 Y. Bai, J. Zhang, Y. Wang, Z. Cao, L. An, B. Zhang, Y. Yu, J. Zhang and C. Wang, *ACS Appl. Nano Mater.*, 2019, **2**(5), 3187–3195.

54 Z. Zheng, X. Liu, G. Huang, H. Chen, H. Yu, D. Feng and D. Qiao, *Friction*, 2021, **10**(9), 1365–1381.

55 D. R. Baer, G. E. McGuire, K. Artyushkova, C. D. Easton, M. H. Engelhard and A. G. Shard, *J. Vac. Sci. Technol., A*, 2021, **39**, 021601.

56 P. S. Bagus, C. J. Nelin, C. R. Brundle, B. V. Crist, N. Lahiri and K. M. Rosso, *J. Chem. Phys.*, 2021, **154**, 094709.

57 T. R. Gengenbach, G. H. Major, M. R. Linford and C. D. Easton, *J. Vac. Sci. Technol., A*, 2021, **39**, 013204.

58 L. Guo, Y. Zhang, G. Zhang, Q. Wang and T. Wang, *Tribol. Int.*, 2021, **153**, 106588.

59 Z. Huang and W. Zhao, *Prog. Org. Coat.*, 2020, **148**, 105881.

60 Y. Zhu, H. Li, J. Fei, C. Li, S. Ma, X. Cai and B. Li, *Tribol. Int.*, 2022, **168**, 107429.

61 J. Liu, X. Wang, Y. Liu, X. Liu and K. Fan, *Carbon*, 2022, **188**, 166–176.

62 X. Liu, Z. Huang, W. Tang and B. Wang, *Nano*, 2017, **12**(09), 41–52.

63 B. Wang, W. Tang, H. Lu and Z. Huang, *J. Mater. Chem. A*, 2016, **4**(19), 7257–7265.

64 T. Khan, Y. Tamura, H. Yamamoto, A. Morina and A. Neville, *J. Tribol.*, 2021, **143**(1), 011705.

65 C. He, S. E, H. Yan and X. Li, *Chin. Chem. Lett.*, 2021, **32**(9), 2693–2714.

66 C. He, H. Yan, X. Li and X. Wang, *Green Chem.*, 2019, **21**(9), 2279–2285.